Int. J. Electrochem. Sci., 17 **(2022)** Article Number: 220656, doi: 10.20964/2022.06.66

International Journal of
ELECTROCHEMICAL
SCIENCE
www.electrochemsci.org

Effect of Nitrogen Content on the Corrosion Resistance of High-nitrogen Austenitic Stainless Steel for Nonmagnetic Drill Collar in a Harsh Service Environment

Guang-Hui Wang, Yue-Qiu Jiang, Ce-An Guo[*]

School of Equipment Engineering, Shenyang Ligong University, Shenyang 110159, China
[*]E-mail: wgh860625@163.com

Received: 31 January 2022 / *Accepted:* 4 April 2022 / *Published:* 7 May 2022

In this work, the effect of N content on the corrosion resistance of high-nitrogen austenitic stainless steels for nonmagnetic drill collars in a harsh service environment was investigated by immersion tests in simulated service environment and XPS analysis. The number and morphology of corrosion pits on 0.63N, 0.79N and 0.83N steels were evaluated using the methods of probability and statistics. The composition of the passive films on 0.63N and 0.83N steels was analysed by XPS, and the mechanism of high N content improving corrosion resistance was discussed. The results show that increasing the N content not only reduced the number of pits but also greatly limited the growth of pit width and depth. In addition, it made pits more likely to appear as a relatively less harmful "shallow disk". The XPS analysis results show that N increased the ratio of chromium oxides and iron oxides in the passive film and promoted the enrichment of CrN, which was beneficial to improving the stability and protection ability of the passive film. This work provides some experience and inspiration for the development of high-nitrogen austenitic stainless steel for nonmagnetic drill collars.

Keywords: high-nitrogen austenitic stainless steel; nonmagnetic drill collars; pitting; passive film; Cl^--H_2S-CO_2 corrosion

1. INTRODUCTION

Nonmagnetic drill collars are important tools for oil and gas field development. They can increase the counterweight of the drill bit and prevent the measuring equipment from interference by the magnetic field during the drilling process[1, 2]. However, the service environment of nonmagnetic drill collars is very harsh. During the drilling process, they are affected not only by high temperature and stress (such as bending, extrusion and torsion) but also by the oil, drilling mud and natural gas[3-5]. The composition of some drilling fluids is more complex and contains aggressive components, including H_2S, CO_2 and Cl^-. These components can easily induce pitting and stress corrosion, which eventually lead to the cracking of nonmagnetic drill collars[6], reduce the life of drill collars and increase the production costs.

The initial materials for nonmagnetic drill collar were AISI-300 series stainless steels equipped with Monel alloy, however, they were replaced because of the low strength and high cost. Afterwards, the nitrogen alloyed austenitic stainless steels, such as Gammaloy Cr-Mn steel, were put into service [1]. With the development of metallurgical technology and materials science, the nitrogen content in Cr-Mn-N nonmagnetic drill collar steels, including DNM140, P550, etc., were gradually increased [6, 7], providing high strength, good toughness and high corrosion resistance [7].

The effect of nitrogen on the corrosion resistance of stainless steels has been widely reported[8-13]. The research by Lee et al. [14] showed that N addition could inhibit the metastable pitting corrosion of stainless steel. In addition, the point defect density of the passive film was reduced[15] and the enrichment of Cr in the passive film was improved by N[16]. In addition, after N alloying, the formation of ammonia (NH_4^+ and NH_3) on the surface of the passive film and the enrichment of CrN in the film favoured the self-healing process of the passive film [10, 16, 17]. Therefore, N can significantly enhance the repassivation ability and corrosion resistance of stainless steels (especially in chloride solution). On the other hand, the addition of N, which can stabilize the austenite phase, is helpful to reduce the content of Ni in austenitic stainless steels, thereby saving costs[18, 19]. However, until now, the influence of a high N content (especially higher than 0.6 wt.%) on corrosion resistance of austenitic stainless steel used for nonmagnetic drill collars in service environments has rarely been reported. Therefore, it is of great importance to study the effect of N content on the pitting corrosion resistance of nonmagnetic drill collars.

This study employed a high-temperature high-pressure reactor to simulate the service environment of nonmagnetic drill collars. Confocal laser scanning microscopy (CLSM) combined with X-ray photoelectron spectroscopy (XPS) analyses were used to systematically study the influence of N content on the corrosion behaviour of high-nitrogen austenitic stainless steels used for nonmagnetic drill collars in a simulated service environment. This work provides some meaningful suggestions for the material selection for nonmagnetic drill collars.

2. EXPERIMENTAL

2.1 Materials preparation

The high-nitrogen austenitic stainless steels investigated in this study were melted in a pressurized induction furnace. Different N contents were achieved by adding nitride alloys and injecting high-purity nitrogen to high pressure. The ingots were then forged into thick plates with dimensions of 120 mm × 30 mm within the temperature range of 900~1200 ℃. The samples for the immersion corrosion tests were cut from the plates with the test surface parallel to the forging direction. Finally, the samples were solution-treated at 1100 ℃ for 1 h, followed by water quenching. The test steels were named according to the N contents, and the chemical compositions are shown in Table 1.

Table 1. Chemical compositions of the test steels (wt.%).

Steels	C	Si	Mn	Cr	Ni	Mo	N	Fe
0.63N	0.013	0.30	21.54	18.50	1.46	0.66	0.63	Bal.
0.79N	0.010	0.32	21.52	18.47	1.49	0.63	0.79	Bal.
0.86N	0.011	0.32	21.58	18.48	1.46	0.65	0.86	Bal.

2.2 Potentiodynamic polarization tests

The potentiodynamic polarization tests in 3.5 wt.% NaCl solution at 40 ℃ were performed on a Reference 600 potentiostat (Gamry) equipped with a conventional three-electrode system, with saturated calomel electrode (SCE) as reference electrode, platinum plate as counter electrode and specimen (1 cm^2) as working electrode. The specimens were ground to 2000 grit using SiC paper.

2.3 High-temperature and high-pressure immersion corrosion test

The high-temperature and high-pressure reactor was employed to simulate the high-temperature and high-pressure service conditions of nonmagnetic drill collars[20]. This equipment mainly consisted of an autoclave, thermocouple, heating jacket, air inlet/outlet, safety valve, rotating cage and stirring motor, etc. The reactor was made of 316L stainless steel, the capacity was 5 L, the maximum experimental temperature was 250 ℃, and the maximum pressure was 10 MPa. Meanwhile, the rotating cage could be driven by a stirring motor to simulate the dynamic conditions. The maximum speed of the rotating cage was 1000 $r \cdot min^{-1}$, and the flow velocity of the liquid on the sample surface was approximately 5 $m \cdot s^{-1}$.

The high-temperature and high-pressure immersion corrosion experiments were carried out in accordance with ASTM G31-72-2004[21]. To simulate the service environment of high-nitrogen austenitic stainless steels for nonmagnetic drill collars, the solution selected was a 3.5% NaCl solution at 120 ℃ with 0.2 MPa H_2S+0.5 MPa CO_2 injected into the reactor. The rotating speed of the stirring motor was set as 350 $r \cdot min^{-1}$, and the flow velocity of the liquid on the sample surface was approximately 1.75 $m \cdot s^{-1}$.

The sample size of high-nitrogen austenitic stainless steels for nonmagnetic drill collars used for high-temperature and high-pressure immersion corrosion tests was 10 mm × 50 mm × 3 mm. The surfaces of the samples were wet ground to 2000 #, cleaned with deionized water and ethanol, and then dried in hot air. Afterwards, their weights were measured using an analytical balance. The samples were soaked in the high-temperature and high-pressure reactor for 30 days. The corrosion products were removed according to ISO 8407-2009[22], and then the samples were weighed again. The corrosion rate was calculated by Eq. 1.

$$V_C = \frac{87600(W_0 - W_1)}{t\rho a} \quad (1)$$

where V_C is the corrosion rate ($mm \cdot a^{-1}$), W_0 and W_1 are the weights of the sample before and after the immersion test (g), t is the immersion time (h), ρ is the density of test steel ($g \cdot cm^{-3}$), and a is the surface area of the sample (cm^2).

2.4 Corrosion morphology observation

A digital camera was used to record the macroscopic morphology of the samples after the immersion test. The pits on the samples were observed by field-emission scanning electron microscopy (FE-SEM, Zeiss Ultra Plus), and the composition of the corrosion products was analysed by energy dispersive spectroscopy (EDS). A confocal laser scanning microscope (CLSM, Olympus OLS4100) was

utilized to observe the pits on the sample after the corrosion products were removed. First, the entire sample surface was scanned under a low magnification to determine the position where pitting corrosion occurred. Then, the magnification was increased to detect the size of the pit, including the depth (*h*) and width (*d*). Because of the irregular shape of the pit, only the maximum depth and width were recorded.

Generally, pitting corrosion occurred randomly, and pits with different sizes were randomly distributed on the samples. Therefore, ten pits were randomly selected for each sample, and the average value was calculated.

2.5 XPS analyses

X-ray photoelectron spectroscopy (XPS) was utilized to detect the composition of the passive film on test steels after high-temperature and high-pressure corrosion tests. Once the samples were taken out of the high-temperature and high-pressure reactor, they were washed with deionized water and ethanol and then dried in hot air. An ESCALAB 250 (Thermo Scientific) equipped with a monochromatic Al Kα (1500 eV, 150 W) X-ray source was used to perform a full-spectrum scan for the passive film to analyse the elemental composition of the passive film. Argon ion sputtering (pressure 1.33×10^{-5} Pa, energy 2 keV, current density 2.0 $\mu A\cdot cm^{-2}$, sputtering area 2 mm × 2 mm) was used to obtain the depth distribution information of the passive film. The spectra of Cr 2p, Fe 2p, Mn 2p, Mo 3d, O 1s, N 1s, Cl 1s and S 1s of the passive film after sputtering for different times were acquired. XPSPEAK software was used to analyse the XPS spectra, and the binding energies of film compositions were obtained by an XPS database[23]. Peak identification was conducted according to the binding energy of the C 1s peak (284.6 eV).

3. RESULTS & DISCUSSION

3.1 Potentiodynamic polarization curves

Figure 1 shows the potentiodynamic polarization curves of the experimental nonmagnetic drill collar steels in 3.5 wt.% NaCl solution at 40 ℃. Massive current fluctuations were observed on the curve of 0.63N steel, which indicates the severe metastable pitting corrosion. In addition, the pitting potential of the 0.63N steel was very low. With increasing the nitrogen content to 0.79 wt.% and 0.86 wt.%, the current fluctuation, i.e. metastable pitting corrosion, was significantly reduced. Moreover, the pitting potentials were substantially enhanced. The potentiodynamic polarization results indicate that the increase in nitrogen content significantly improved the corrosion resistance of nonmagnetic drill collar steels.

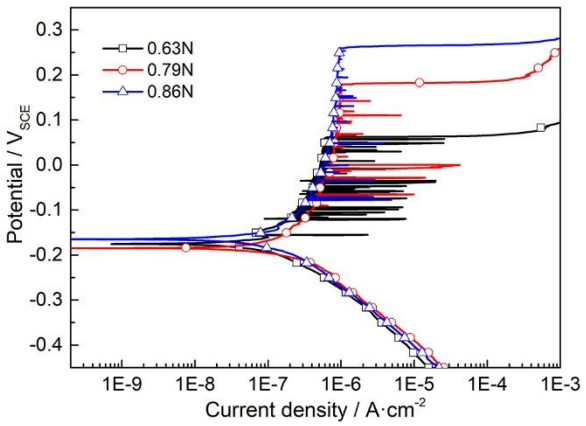

Figure 1. The potentiodynamic polarization curves of the experimental nonmagnetic drill collar steels in 3.5 wt.% NaCl solution at 40℃.

3.2 Immersion corrosion weight loss analyses

To investigate the corrosion resistance of test steels in the simulated service environment of nonmagnetic drill collars, the corrosion rates (V_C) of test steels in the simulated service environment were calculated according to Eq. 1, as listed in Table 2. The V_C values for the three test steels are all very small. As the N content increased, the V_C of the test steels decreased from 3.87×10^{-3} mm·a^{-1} to 2.55×10^{-3} mm·a^{-1} and 2.27×10^{-3} mm·a^{-1}. The results indicate that increasing the N content can enhance the corrosion resistance of high-nitrogen austenitic stainless steels used for nonmagnetic drill collars in a simulated service environment.

Table 2. Corrosion rates (V_C) of the test steels in simulated service environment.

Steels	**0.63N**	**0.79N**	**0.86N**
V_C/(mm·a^{-1})	3.87×10^{-3}	2.55×10^{-3}	2.27×10^{-3}

3.3 Surface corrosion morphology observation

The corrosion products of the test steels after the immersion tests were removed, and the macroscopic corrosion morphologies are shown in Figure 2. A layer of yellow corrosion scale is attached to the surface of the three test steels, and the edges of the samples also suffer corrosion. Nevertheless, there is no obvious large pit on the samples. Since the corrosion rates of the test steels during the immersion test were relatively low, no significant difference could be observed in the macroscopic corrosion morphologies of the three test steels.

Figure 2. Macroscopic corrosion morphology of the steels after immersion and removing corrosion products: (a) 0.63N; (b) 0.79N; (c) 0.86N.

To observe the morphologies of pits more clearly, CLSM was used to observe the surface of the samples at the microscale, and the sizes of ten pits were randomly measured and recorded, including the depth (h) and width (d). The average depth ($\bar{h}$), average width ($\bar{d}$), maximum depth (h_{max}) and maximum width (d_{max}) of the pits are listed in Table 3. The average depths of the pits on the three test steels are 14.96 μm, 11.35 μm, and 4.22 μm, and the average widths are 37.57 μm, 33.68 μm, and 21.17 μm, respectively. With the increase in N content, the values of $\bar{h}$ and $\bar{d}$ of the pits on the test steels gradually decreased, indicating that the corrosion resistance of the test steels under the simulated service environment was gradually improved by N. Additionally, the standard deviations of $\bar{h}$ and $\bar{d}$ of the pits also decreased with the increase in N content, indicating that the size of pits on the steel with a lower N content is more random, and more deep and wide pits formed. Increasing the N content inhibited the growth of the pits and reduced their depth and width.

Table 3. Depth and width of the pitting of the test steels after removing corrosion products.

Steels	$\bar{h}$/μm	h_{max}/μm	$\bar{d}$/μm	d_{max}/μm
0.63N	14.96±12.74	35.76	37.57±30.32	97.07
0.79N	11.35±11.53	33.76	33.68±27.78	76.20
0.86N	4.22±3.76	12.63	21.17±9.71	35.40

The macroscopic corrosion morphologies of the largest pits on the three test steels are shown in Figure 3(a)~(c). The widths of the largest pits are 97.07, 76.20 and 35.40 μm for 0.63N, 0.79N and 0.86N steels, respectively. There are two large pits on 0.79N steel close to each other, but their depths and widths are both smaller than those of 0.63N steel. Therefore, increasing the N content significantly reduces the depth and width of the largest pits on the test steels. The 3D corrosion morphologies of the largest pits after removing the corrosion products are shown in Figure 3(d)~(f). The depths of the largest pits on the three test steels are 35.76 μm, 33.76 μm, and 12.63 μm for the 0.63N, 0.79N and 0.86N steels, respectively. The depths of the maximum pits on 0.86N steel are much smaller than those on the 0.63N and 0.79N steels, which indicates that the higher N content reduced the tendency of pits to develop at depth.

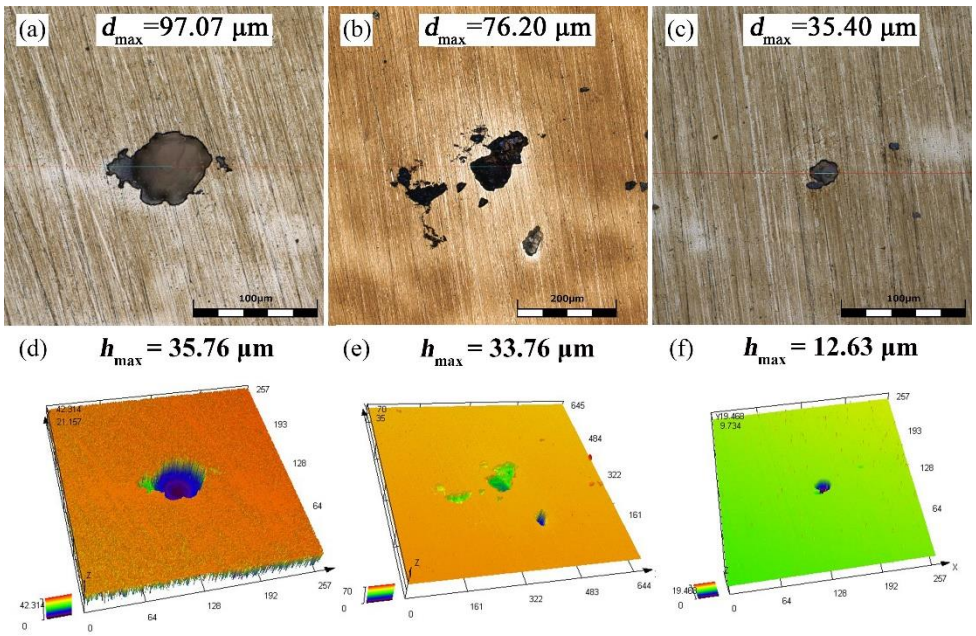

Figure 3. Corrosion morphologies and 3D images of the maximum pits on the test steels: (a)(d) 0.63N; (b)(e) 0.79N; (c)(f) 0.86N.

To analyse the composition of corrosion products, FE-SEM was used to observe the corrosion morphology of 0.63N steel. Figure 4 shows that the corrosion products mainly contain C and S, indicating that CO_2 and H_2S in the simulated service environment would participate in the corrosion process and deteriorate the corrosion resistance of the test steels.

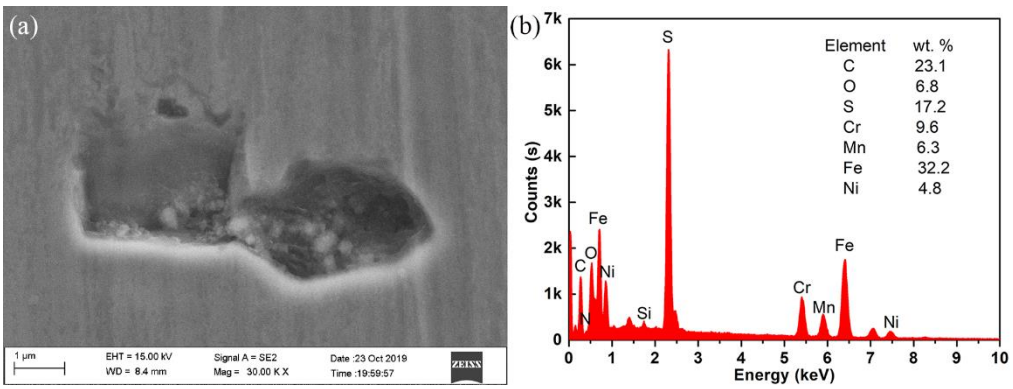

Figure 4. (a) Morphology and (b) EDS results of pit on 0.63N steel in simulated service environment.

In recent years, CO_2 corrosion has caused huge losses to the oil and natural gas industries and has therefore gradually attracted much attention[20, 24, 25]. In a CO_2-saturated solution, an electrochemical corrosion process would occur on the surface of stainless steel, shown as the following reaction:

$$Fe+CO_2+H_2O=FeCO_3+H_2 \quad (2)$$

The final product of this reaction is $FeCO_3$ (which might eventually form Fe_3O_4 at high temperatures), which would destroy the passive film on the surface of the test steels. According to Eq. 3 and 4, N could increase the pH value inside the initial pits, neutralize the H_2CO_3 in the solution, and slow down the formation progress of $FeCO_3$ (Eq. 2). Therefore, increasing the N content can alleviate CO_2 corrosion to a certain extent, thereby improving the corrosion resistance of high-nitrogen austenitic stainless steel in a CO_2-saturated solution.

$$[N]+3H^{+}+3e^{-}=NH_3 \tag{3}$$

$$[N]+4H^{+}+3e^{-}=NH_4^{+} \tag{4}$$

Furthermore, for H_2S corrosion, the presence of H_2S would also aggravate the corrosion of stainless steels[26, 27]. H_2S could destroy the passive film, thus accelerating the pitting corrosion of stainless steels. Additionally, H_2S undergoes a dissociation reaction through Eq. 5 and 6. The products HS^{-} and S^{2-} could easily adsorb on the surface of the test steels and form an adsorbed complex ion $Fe(HS^{-})_{ads}$ with the Fe matrix. At the same time, the adsorbed HS^{-} and S^{2-} could induce a more negative corrosion potential of the steel, thereby accelerating the cathodic hydrogen evolution reaction. Since H^{+} is a strong depolarizer, it is easy for H^{+} to gain electrons at the cathode, which weakens the metal bond between Fe atoms, thus promoting anodic dissolution and accelerating the corrosion of stainless steels. Since N could increase the pH value inside the pit cavities, increasing the N content would also restrain the H_2S corrosion of high-nitrogen austenitic stainless steels.

$$H_2S_{(aq)} \rightleftharpoons H^{+}+HS^{-} \tag{5}$$

$$HS^{-} \rightleftharpoons H^{+}+S^{2-} \tag{6}$$

3.4 Statistical analyses of pitting

To analyse the effect of N content on the corrosion resistance of test steels in the simulated service environment in more detail, the sizes of ten pits were measured by CLSM. The cumulative probability of the pit size (taking the depth (h) as an example) was obtained based on Eq. 7 [28, 29]:

$$F(x)=\frac{n}{N+1} \tag{7}$$

where $F(x)$ is the probability when the size of the pit is less than or equal to x μm, n is the sequence number of the pit depth (arranged from small to large), and N is the number of investigated pits.

Furthermore, the *Gumbel* distribution of pit depth was calculated by Eq. 8 and 9 [29, 30]:

$$F(x)=\exp\left\{-\exp\left[-\frac{(h_i-\mu)}{\alpha}\right]\right\} \tag{8}$$

$$-\ln[-\ln F(x)]=\frac{d_i-\mu}{\alpha} \tag{9}$$

where h_i is the depth of the pit (μm), α is the scale parameter (μm), and μ is the central parameter (μm).

The probability distribution of pitting was calculated by the double exponential equation, shown as Eq. 10 and 11 [31]:

$$P(x)=1-\exp\left\{-\exp\left\{-\frac{[h_i-(\mu+\alpha\ln S)]}{\alpha}\right\}\right\} \quad (10)$$

$$P(x)_{max}=\mu+\alpha\ln S \quad (11)$$

where $P(x)$ represents the probability when the pit depth is x μm, S is the surface area of the sample (mm^2), and P_{max} is the probability when the maximum pit depth is x μm.

In addition, according to the statistical size of pits (depth (h) and width (d)), the types of pits could be further classified [20]. When $d/2h>1$, the pit was categorized as the "shallow disk type"; when $d/2h=1$, the pit was categorized as the "hemispherical type"; when $d/2h<1$, the pit was categorized as the "bullet type".

Figure 5(a) shows the cumulative probability of the pit depth of the test steels after 30 days of immersion. The pit depth of 0.63N steel is between 3.91~35.76 μm, while those of 0.79N and 0.86N steels are between 1.95~33.76 and 1.42~12.63 μm, respectively. This suggests that with increasing N content, especially when it reaches 0.86 wt.%, the depth of pits on the test steels can be significantly reduced.

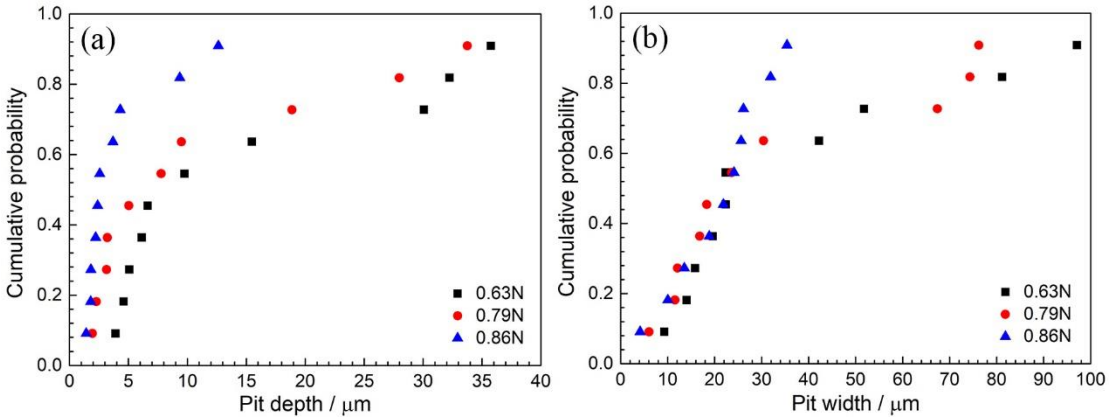

Figure 5. Cumulative probability plots of (a) depth and (b) width of the pits on the test steels after immersion corrosion for 30 days.

Figure 5(b) shows the cumulative probabilities of the pit width after the test steels were immersed for 30 days. The pit depth of the 0.63N steel is between 9.30~97.07 μm, the depth of 0.79N steel is between 6.03~76.20 μm, and the depth of 0.86N steel is evidently decreased to 4.16~35.40 μm. Therefore, increasing the N content can significantly reduce the width of the pits. However, between 4~25 μm, the scatters of the three steels are very close to each other, and the pit width does not decrease monotonously with increasing N content. In contrast, the pit depth is reduced by increasing the N content under all cumulative probabilities in Figure 5(a). This result manifests that the increasing N content would lead to the presence of shallower pits, namely, improving the corrosion resistance of the test steels.

The *Gumbel* distribution curve of the pit depth of the test steels after immersion for 30 days is shown in Figure 6(a), and the *Gumbel* distribution parameters are listed in Table 4. The *Gumbel* distribution curves of the pit depths exhibited two linear regions. Generally, two linear regions represent

two kinds of pitting behaviours controlled by two different corrosion mechanisms [29]. The pits with shallower depths were preferentially caused by Cl^--corrosion, and most of them were metastable. For pits with larger depths, in addition to Cl^--corrosion, corrosion caused by CO_2 and H_2S was also induced. Therefore, the metastable pits that emerged at this moment could easily transform into stable pits. The *Gumbel* distribution curves of the pit width are shown in Figure 6(b). The 0.63N and 0.79N steels exhibit two linear regions, while only one linear region is observed for the 0.86N steel. The results show that the pits on the 0.86N steel were much smaller and shallower than those on the 0.63N and 0.79N steels.

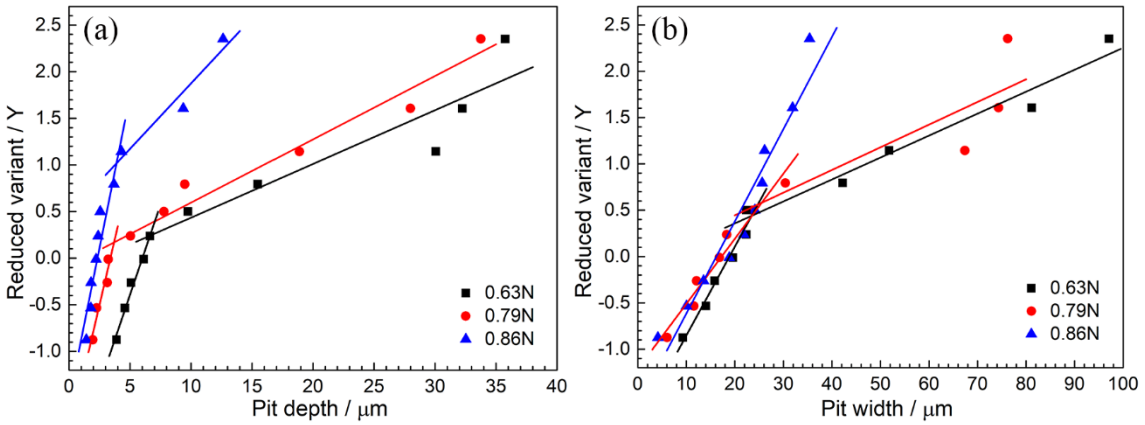

Figure 6. *Gumbel* probability plots of (a) depth and (b) width of the pits on the test steels after immersion corrosion for 30 days.

Table 4. *Gumbel* distribution parameters of the pit depth and width.

Steels	α_h	μ_h	α_h'	μ_h'	α_d	μ_d	α_d'	μ_d'
0.63N	2.58	6.01	17.36	2.46	10.42	18.89	42.21	4.93
0.79N	1.78	3.39	14.74	1.23	14.23	17.29	40.87	1.84
0.86N	1.53	2.33	7.13	-3.36	10.05	16.19	-	-

According to the *Gumbel* distribution parameters in Table 4, the probability distribution of stable pits formed after 30 days of immersion could be obtained based on Eq. 1 and 7~9, as shown in Figure 7. In the low pit depth region (as shown in the enlarged image in Figure 7(a)), the probabilities of pitting corrosion for the three test steels are all close to 1, and the pits at this moment are usually initiated pits or metastable pits. However, as the pit depth increased, the probability of pitting corrosion gradually decreased, and the pits at this moment were usually stable. Furthermore, as the N content increased, the probability of stable pitting corrosion was significantly reduced, indicating that the pitting corrosion resistance of the test steels was significantly enhanced. The probability distributions of the pit width are shown in Figure 7(b). The probability was also reduced by increasing the N content. As shown in the enlarged view of Figure 7(b), in the region of large pit width, the pitting corrosion probability of the 0.79N steel is slightly lower than that of the 0.63N steel, while the pitting corrosion probability of the

0.86N steel drops dramatically. Therefore, increasing the N content decreased the probability of stable pitting corrosion of the test steels in the simulated service environment, especially for the high N addition of 0.86 wt.%.

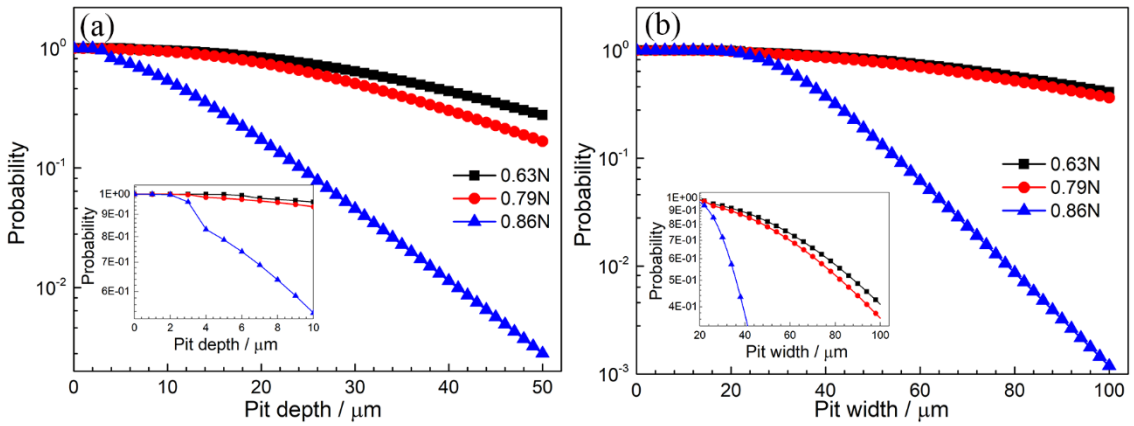

Figure 7. Probabilities of various pit (a) depth and (b) width of the test steels after immersion corrosion for 30 days.

To study the effect of N content on the shape of pits formed on the test steels, the geometrical shape was obtained according to the sizes of the pits, as shown in Figure 8. The results show that among the ten investigated pits, there are two "bullet type" ($d/2h<1$) pits on the 0.63N steel, one "hemispherical type" ($d/2h=1$) pit on the 0.79N steel, and one "hemispherical type" pit on 0.86N steel, while the remainders are all "shallow disk type" pits ($d/2h>1$). As the N content increases, the value of $d/2h$ exhibits a decreasing trend.

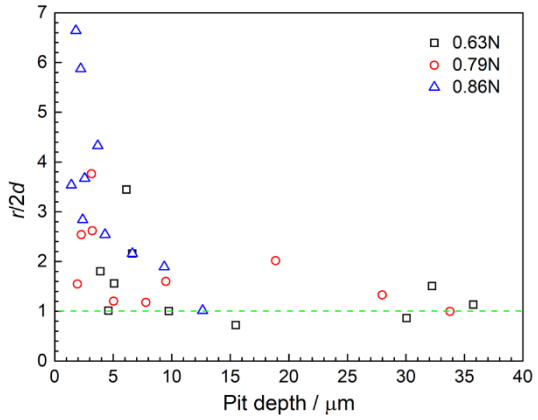

Figure 8. Geometrical shapes of the pits on the test steels after immersion for 30 days.

It is generally believed that the damage of pitting corrosion decreases as the pit depth decreases. In other words, the "bullet type" pits are the most harmful, the "hemispherical type" pits are the second harmful, and the "shallow disk type" pits are relatively mild [20]. Therefore, with the increase in N content, the pits on the high-nitrogen austenitic stainless steel became shallower. The pits on the 0.86N

steel were much smaller than those on the 0.63N and 0.79N steels, indicating that less harm would be generated by increasing N content.

3.5 XPS analysis

The passive film formed on the surface of the 0.63N and 0.86N steels after immersion in the simulated service environment for 30 days was studied to clarify the influence of N content on the corrosion behaviour of the test steels. The XPS full spectra in Figure 9 show the existence of C, N, O, Cr, Mn and Fe peaks on the surface of the two test steels. Because the Ni and Mo contents in the steels are very low, the corresponding peaks are not detected.

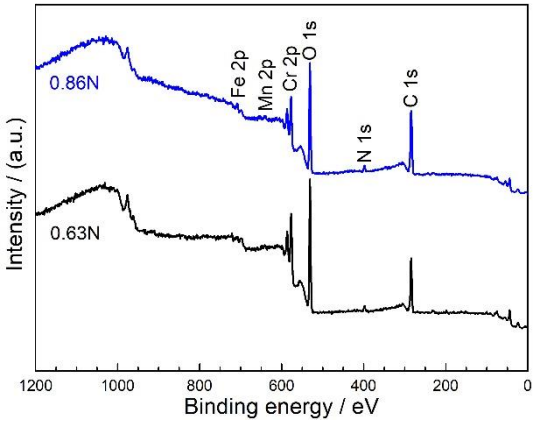

Figure 9. XPS survey spectra of the passive films on the test steels after immersion for 30 days.

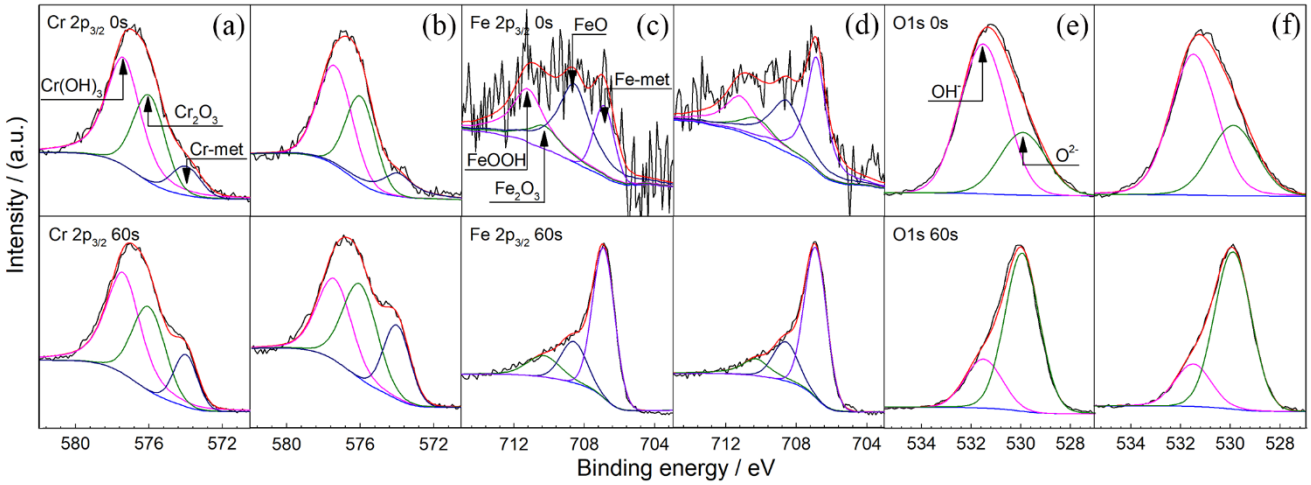

Figure 10. XPS spectra of Cr $2p_{3/2}$, Fe $2p_{3/2}$ and O 1s of the passive film after sputtering for 0 and 60 s: (a)(c)(e) 0.63N; (b)(d)(f) 0.86N.

The XPS spectra of Cr $2p_{3/2}$, Fe $2p_{3/2}$ and O 1s with etching times of 0 and 60 s are shown in Figure 10. The spectrum of Cr $2p_{3/2}$ is divided into three peaks ($Cr(OH)_3$ (577.4±0.1 eV), Cr_2O_3 (576.2±0.1 eV) and Cr-met (573.4±0.2 eV)). The spectrum of Fe $2p_{3/2}$ is divided into four peaks (FeOOH (711.2±0.1 eV), Fe_2O_3 (709.9±0.1 eV), FeO (708.3±0.1 eV) and Fe-met (706.6±0.1 eV)). The spectrum

of O 1s is divided into two peaks (OH^-(531.3±0.1 eV) and O^{2-}(529.9±0.1 eV)). After the peak separation treatment, it can be seen that the outer layer of the passive film is mainly composed of hydroxides, while the inner layer mainly consists of oxides.

Table 5 shows the ratio of oxides to hydroxides in the passive films with etching times of 0 and 60 s. At the outermost surface of the passive film, as the N content increases from 0.63 wt.% to 0.86 wt.%, the ratios of $Cr_2O_3/Cr(OH)_3$, $(Fe_2O_3+FeO)/FeOOH$, Fe_2O_3/FeO and O^{2-}/OH^- all increase. After sputtering for 60 s, FeOOH disappeared. Increasing the N content improves the ratios of $Cr_2O_3/Cr(OH)_3$, Fe_2O_3/FeO and O^{2-}/OH^-, thereby enhancing the stability and protective ability of the passive film and optimizing the corrosion resistance of test steels [32, 33].

Table 5. Ratios of oxides with hydroxides, and oxides with different valence states in the passive films after sputtering for 0 and 60 s.

Steels/sputtering time	$Cr_2O_3/Cr(OH)_3$	$(Fe_2O_3+FeO)/FeOOH$	Fe_2O_3/FeO	O^{2-}/OH^-
0.63N-0 s	0.61	1.90	0.29	0.42
0.86N-0 s	0.74	2.02	0.39	0.49
0.63N-60 s	0.66	-	0.56	3.09
0.86N-60 s	1.09	-	0.64	3.62

The XPS spectra of Mo 3d and Mn $2p_{3/2}$ in the passive film after sputtering for 0 and 60 s are shown in Figure 11. At the outermost surface of the passive film, no obvious peaks of Mo 3d and Mn $2p_{3/2}$ are observed. When sputtered for 60 s, the spectrum of Mo 3d can be divided into six peaks (Mo^{6+} (235.7±0.1 eV and 232.5±0.1 eV), Mo^{4+} (232.7±0.1 eV and 229.5±0.1 eV) and Mo-met (230.8±0.1 eV and 227.7±0.1 eV)). The spectrum of Mn $2p_{3/2}$ is divided into three peaks (MnO_2 (642.4±0.1 eV), MnO (640.4±0.1 eV) and Mn-met (638.5±0.1 eV)). Since the Mo contents in the two test steels are very close, the influence of Mo on the passive film is not obvious in the present work. Additionally, Mn mainly exists in the form of MnO_2 and MnO in the inner layer of the passive film. Yang et al.[34] reported that Mn significantly deteriorated the corrosion resistance of a CoFeNiCr high entropy alloy by suppressing the passivation process. In addition, the existence of Mn in the passive films prominently reduced the stability of the passive film. However, the Mn spectra of the 0.63N and 0.86N steels did not exhibit obvious differences due to the same Mn content.

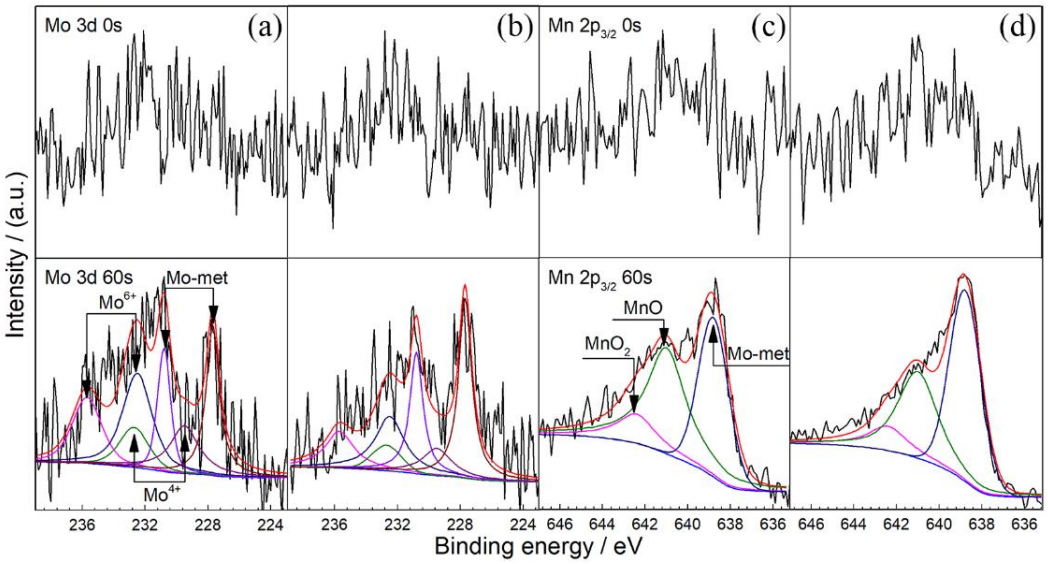

Figure 11. XPS spectra of Mo 3d and Mn $2p_{3/2}$ in the passive films after sputtering for 0 and 60 s: (a)(c) 0.63N; (b)(d) 0.86N.

The XPS spectra of N 1s in the passive film after sputtering for 0, 20, and 60 s are shown in Figure 12. The spectrum of N 1s can be divided into four peaks (NH_4^+ (400.8±0.1 eV), NH_3 (399.6±0.1 eV), Cr_2N (397.6±0.1 eV) and CrN (396.8±0.1 eV)). Cr_2N is distributed throughout the passive film. Ammonia (NH_4^+ and NH_3) is mainly concentrated on the outer surface of the passive film. The presence of ammonia indicates that N might dissolve and then form NH_4^+ and NH_3 by consuming H^+ in the solution, thereby increasing the pH value near the passive film.

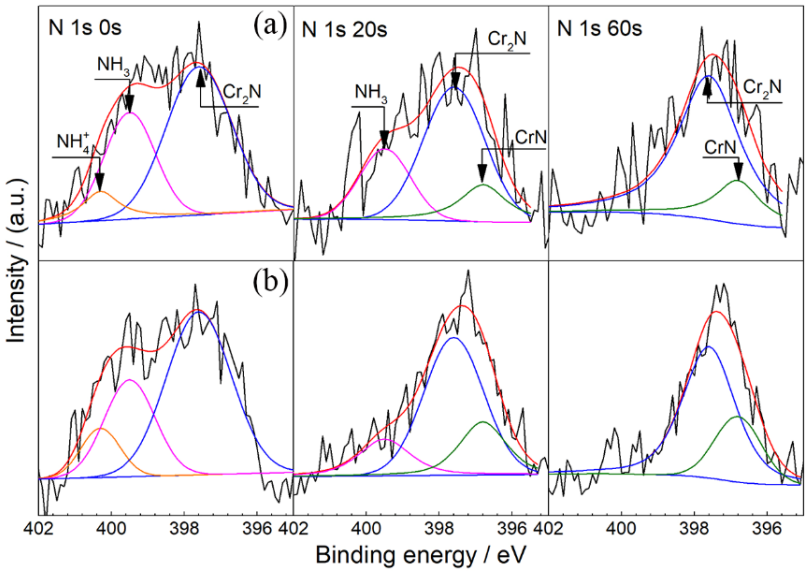

Figure 12. XPS spectra of N 1s in the passive films after sputtering for 0, 20 and 60 s: (a) 0.63N; (b) 0.86N.

This could inhibit the damage of the passive film and promote the repassivation of metastable

pits [15, 35]. With a sputtering time of 20 s, the peak corresponding to NH_4^+ disappears, and only a small amount of NH_3 remains, while the peak representing CrN emerges. With further sputtering to 60 s, the peak corresponding to NH_3 also disappears, and the N 1s spectrum is mainly composed of Cr_2N and CrN.

Table 6 shows the ratios of CrN to Cr_2N in the passive film after sputtering for 20 and 60 s. Increasing the N content from 0.63 wt.% to 0.86 wt.% raises the ratios of CrN to Cr_2N. It is widely accepted that CrN can promote the self-healing process of passive films by forming Cr_2O_3 based on the reaction shown in Eq. 12. In addition, CrN in the passive film/metal interface is also beneficial for improving the stability and protection of the passive film [16, 17, 36]. Therefore, increasing the N content increased the proportion of CrN in the inner layer of the passive film and thus improved the corrosion resistance of the steels.

$$2CrN+3H_2O_{ads}=Cr_2O_3+2NH_3(ligands) \quad (12)$$

Table 6. The ratios of CrN to Cr_2N in the passive films after sputtering for 20 and 60 s.

Steels	20 s	60 s
0.63N	0.30	0.25
0.86N	0.36	0.37

Figure 13 shows the XPS spectra of Cl 1s in the passive film after sputtering for 0, 20 and 60 s. The Cl 1s peaks were detected at different depths of the passive film on the 0.63N steel, but no obvious Cl 1s peaks were detected in that on the 0.86N steel. This suggested that a high N content could restrain the permeation and internal diffusion of Cl^- into the passive film, thus suppressing the Cl^--corrosion of the 0.86N steel. Additionally, the XPS spectra of S 1s are shown in Figure 14. No obvious S 1s peak was detected, which indicated that both the 0.63N and 0.86N steels could defend against the attack of H_2S corrosion in the simulated service environment of nonmagnetic drill collars.

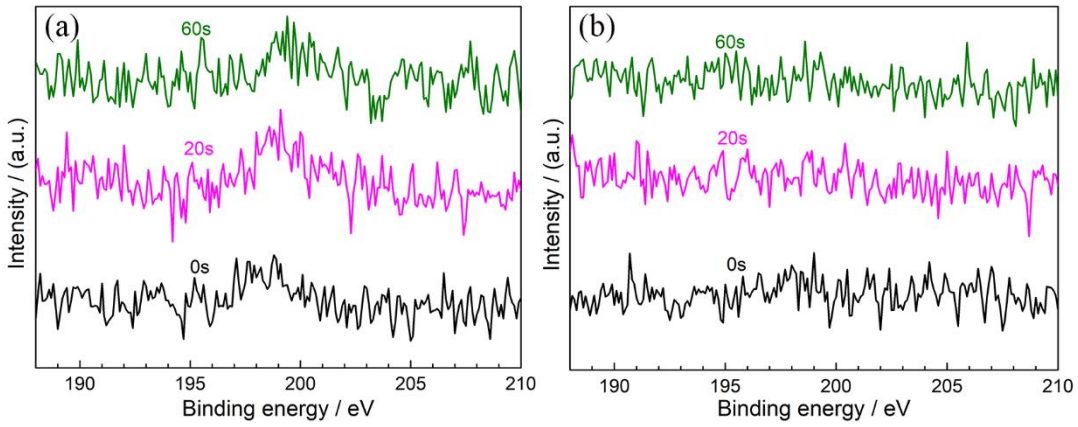

Figure 13. XPS spectra of Cl 1s in the passive films after sputtering for 0, 20 and 60 s: (a) 0.63N; (b) 0.86N.

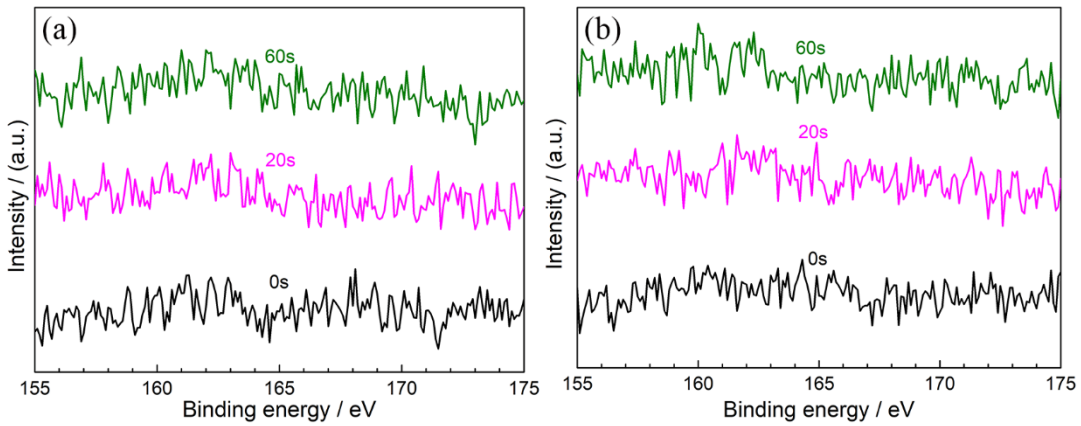

Figure 14. XPS spectra of S 1s in the passive films after sputtering for 0, 20 and 60 s: (a) 0.63N; (b) 0.86N.

4. CONCLUSION

The effect of N content on the corrosion behaviour of high-nitrogen austenitic stainless steels for nonmagnetic drill collars in a simulated service environment was investigated. The main conclusions are summarized as follows:

(1) As the N content increased from 0.63 wt.% to 0.86 wt.%, the corrosion rates of the test steels after 30 days of immersion were reduced, and the depths and widths of the pits both decreased. Additionally, the shape of pits tended to become shallower, indicating that increasing N content could improve the corrosion resistance of the test steels.

(2) In the simulated service environment of nonmagnetic drill collars, Cl^--corrosion imposed a greater threat to the test steels than H_2S-corrosion did. Increasing the N content significantly reduced the permeation and internal diffusion of Cl^- into the passive film and the damage caused by Cl^- corrosion to the test steels.

(3) The increased N content increased the proportion of chromium oxides and iron oxides in the passive film, thereby improving the stability of the passive film. In the outer layer of the passive film, N formed NH_4^+ and NH_3 by consuming H^+ in the solution, thereby inhibiting the damage to the passive film and promoting the repassivation of metastable pits. In the inner layer of the passive film, N promoted the enrichment of CrN, the precursor of the passive film, which was beneficial for improving the stability and protection ability of the passive film.

ACKNOWLEDGEMENTS
The present research was financially supported by the National Science Foundation of Liaoning Province of China (2019-ZD-0264).

References

1. M.J. Knight and F.P. Brennan, *Eng. Fail. Anal.*, 6 (1999) 301.
2. L.W. Xu, H.B. Li, H.B. Zheng, P.C. Lu, H. Feng, S.C. Zhang, W.C. Jiao and Z.H. Jiang, *J. Iron Steel Res. Int.*, 27 (2020) 1466.
3. Z.Q. Zhong, Y.L. Li, Y.C. Liu, L. Bao and Z.L. Tian, *Eng. Fail. Anal.*, 105 (2019) 727.
4. N.A. Mariano and D. Spinelli, *Mater. Sci. Eng. A*, 385 (2004) 212.
5. K.A. Macdonald and H. Aigner, *Eng. Fail. Anal.*, 3 (1996) 281.
6. G. Saller and H. Aigner, *Mater. Manuf. Process.*, 19 (2004) 41.
7. Z.X. Zou, Y.P. Lang and H.P. Qu, *Hot Work. Technol.*, 42 (2013) 6.
8. H.B. Li, Z.H. Jiang, H. Feng, S.C. Zhang, L. Li, P.D. Han, R.D.K. Misra and J.Z. Li, *Mater. Des.*, 84 (2015) 291.
9. H.J. Grabke, *ISIJ Int.*, 36 (1996) 777.
10. R.F.A. Jargelius-Pettersson, *Corros. Sci.*, 41 (1999) 1639.
11. Y. Han, H.B. Li, H. Feng, Y.Z. Tian, Z.H. Jiang and T. He, *Mater. Sci. Eng. A*, 814 (2021) 141235.
12. J.T. Yu, S.C. Zhang, H.B. Li, Z.H. Jiang, H. Feng, P.P. Xu and P.D. Han, *J. Mater. Sci. Technol.*, 112 (2022) 184.
13. P.C. Lu, H.B. Li, H. Feng, Z.H. Jiang, H.C. Zhu, Z.Z. Liu and T. He, *Metall. Mater. Trans. B*, 52 (2021) 2210.
14. J.B. Lee and S.I. Yoon, *Mater. Chem. Phys.*, 122 (2010) 194.
15. S. Ningshen, U. Kamachi Mudali, V.K. Mittal and H.S. Khatak, *Corros. Sci.*, 49 (2007) 481.
16. H. Feng, Z.H. Jiang, H.B. Li, P.C. Lu, S.C. Zhang, B.B. Zhang, T. Zhang, D.K. Xu and Z.G. Chen, *Corros. Sci.*, 144 (2018) 288.
17. H. Feng, H.B. Li, X.L. Wu, Z.H. Jiang, S. Zhao, T. Zhang, D.K. Xu, S.C. Zhang, H.C. Zhu, B.B. Zhang and M.X. Yang, *J. Mater. Sci. Technol.*, 34 (2018) 1781.
18. M. O. Speidel, *Materialwissenschaft and Werkstofftechnik*, 37 (2006) 875.
19. L. Yang, Y.B. Ren and P. Wan, *Sci. China Technol. Sci.*, 55 (2012) 329.
20. Y. Zhao, X. Li, C. Zhang, T. Zhang, J. Xie, G. Zeng, D. Xu and F. Wang, *Corros. Sci.*, 145 (2018) 307.
21. ASTM G31-72, Standard practice for laboratory immersion corrosion testing of metals, ASTM Committee, United States, (2004).
22. ISO 8407, Corrosion of metals and alloys - removal of corrosion products from corrosion test specimens, International Organization for Standardization, Switzerland, (2009).
23. Y. Yang, X. Ning, H. Tang, L. Guo and H. Liu, *Appl. Surf. Sci.*, 320 (2014) 274.
24. J. Li, D.B. Sun, D.J. Yang, M.L. Yan, M.X. Lu and G.X. Zhao, *Iron Steel*, 36 (2001) 48.
25. Z.H. Duan and D.D. Li, *Geochim. Cosmochim. Acta*, 72 (2008) 5128.
26. Z. Wang, Z. Feng and L. Zhang, *Corros. Sci.*, 174 (2020) 108844.
27. M. Javidi, S. Haghshenas and M. Shariat, *Corros. Sci.*, 163 (2019) 108230.
28. T. Zhang, C.M. Chen, Y.W. Shao, G.Z. Meng, F.H. Wang, X.G. Li and C.F. Dong, *Electrochim. Acta*, 53 (2008) 7921.
29. H. Feng, H.B. Li, P.C. Lu, C.T. Yang, Z.H. Jiang and X.L. Wu, *Acta Metall. Sinica*, 55 (2019) 1457.
30. G.Z. Meng, L.Y. Wei, T. Zhang, Y.W. Shao, F.H. Wang, C.F. Dong and X.G. Li, *Corros. Sci.*, 51 (2009) 2151.
31. T. Zhang, X.L. Liu, Y.W. Shao, G.Z. Meng and F.H. Wang, *Corros. Sci.*, 50 (2008) 3500.
32. C.R. Clayton, G.P. Halada and J.R. Kearns, *Mater. Sci. Eng. A*, 198 (1995) 135.
33. H. He, T. Zhang, C.Z. Zhao, K. Hou, G.Z. Meng, Y.W. Shao and F.H. Wang, *J. App. Electrochem.*, 39 (2009) 737.
34. J. Yang, J. Wu, C.Y. Zhang, S.D. Zhang, B.J. Yang, W. Emori and J.Q. Wang, *J. Alloys. Compd.*, 819 (2020) 152943.

35. C.O.A. Olsson, *Corros. Sci.*, 37 (1995) 467.
36. R.D. Willenbruch, C.R. Clayton, M. Oversluizen, D. Kim and Y. Lu, *Corros. Sci.*, 31 (1990) 179